



Full optical characterization of single nanoparticles using quantitative phase imaging

SAMIRA KHADIR,^{1,3} DANIEL ANDRÉN,² PATRICK C. CHAUMET,¹ SERGE MONNERET,¹ NICOLAS BONOD,¹ MIKAEL KÄLL,² ANNE SENTENAC,¹ AND GUILLAUME BAFFOU^{1,*}

¹Institut Fresnel, CNRS, Aix Marseille Université, Centrale Marseille, Marseille, France

²Department of Physics, Chalmers University of Technology, 412 96 Göteborg, Sweden

³e-mail: samira.khadir@fresnel.fr

*Corresponding author: guillaume.baffou@fresnel.fr

Received 29 October 2019; revised 7 January 2020; accepted 14 January 2020 (Doc. ID 381729); published 17 March 2020

This paper introduces a procedure aimed to quantitatively measure the optical properties of nanoparticles, namely the complex polarizability and the extinction, scattering, and absorption cross sections, simultaneously. The method is based on the processing of intensity and wavefront images of a light beam illuminating the nanoparticle of interest. Intensity and wavefront measurements are carried out using quadriwave lateral shearing interferometry, a quantitative phase imaging technique with high spatial resolution and sensitivity. The method does not require any preknowledge on the particle and involves a single interferogram image acquisition. The full determination of the actual optical properties of nanoparticles is of particular interest in plasmonics and nanophotonics for the active search and characterization of new materials, e.g., aimed to replace noble metals in future applications of nanoplasmonics with less-lossy or refractory materials. © 2020 Optical Society of America under the terms of the [OSA Open Access Publishing Agreement](#)

<https://doi.org/10.1364/OPTICA.381729>

1. INTRODUCTION

Nanoparticles (NPs) featuring localized plasmon or Mie resonances have been extensively studied for nanophotonics applications to achieve light confinement at nanoscale [1], enhancement [2,3], scattering [4], heat generation [5], SERS [6], and phase control [7,8]. For these applications, a large variety of materials including highly doped semiconductors [9], oxides, nitrides [10–12], alkali metals [13,14], alloys/intermetallics [15–18], and dielectrics [19], have been proposed recently. Quantifying the optical responses of all these NPs and comparing them with each other is intricate and remains the main issue for the search of better optical materials. To quantitatively estimate the efficiency of a material, or of a NP, simple figures of merit [20] or analytical models can be used for simple geometries, or numerical simulations for complex geometries and environments. However, the material is modeled via its bulk complex permittivity, usually measured on material layers. This approach proved efficient with gold, but may be inappropriate when considering NPs made of other materials, where surface effects dominate or where surface oxidation occurs [21], or for alloys where the theoretical determination of the effective permittivity is not straightforward [22,23].

The optical characterization of individual NPs usually consists in measuring cross sections, which is all the more difficult when the NP is downsized. To effectively extract signal out of noise, most of the experimental techniques are based on the spatial modulation (SM) of a focused laser beam associated with a lock-in detection.

Arbouet *et al.* introduced the SM technique in 2004 to quantitatively retrieve the extinction cross section (σ_{ext}) of single NPs as small as 5 nm in diameter [24]. This approach is quantitative only when absorption is dominant over scattering, since it neglects the portion of scattered light that is not collected. In practice, quantifying only extinction is not enough to fully characterize the optical properties of NPs. Other experimental procedures have been designed to retrieve scattering (σ_{sca}) or absorption (σ_{abs}) cross sections as well [25,26], although these quantities are more difficult to access and to be quantitatively measured. The Link's group reported in 2010 quantitative measurements of both absorption and scattering cross sections of single NPs using two separate techniques, namely dark-field spectroscopy and another SM technique called photothermal imaging [27]. SM techniques have been used to measure absorption and scattering cross sections originating this time from the same signal [28,29]. Recently, the use of an integrating sphere implemented upon an optical microscope has been demonstrated to enable absorption and scattering measurements on single NPs [30,31]. The main drawbacks of all these techniques are that they require expensive equipment such as lasers, modulating elements, and lock-in amplifiers, and they are sensitive to optical alignments. The analysis procedures are also complex and often based on a precise knowledge of the point spread function of the microscope [32]. These drawbacks make SM techniques impractical for routine characterization of NPs [31]. Very recently, Zilli *et al.* introduced a technique aimed to measure all the optical cross sections of individual NPs at once, which is not based on the

use of a focused laser and SM measurements [32]. The technique aims to be simple and requires only a wide-field illumination, a camera, and a standard optical microscope. It consists in successively acquiring and postprocessing bright-field and dark-field images of single NPs. This technique requires a precise characterization of the collection properties of the microscope objective lens.

Even more fundamental than the three cross sections is the complex optical polarizability. For instance, for a dipolar NP, the sole knowledge of its complex optical polarizability α enables the derivation of all the cross sections of the NP at once [33]:

$$\sigma_{\text{ext}} = \frac{k_0}{n} \text{Im}(\alpha), \quad (1)$$

$$\sigma_{\text{sca}} = \frac{k_0^4}{6\pi} |\alpha|^2, \quad (2)$$

$$\sigma_{\text{abs}} = \sigma_{\text{ext}} - \sigma_{\text{sca}}, \quad (3)$$

where k_0 is the free-space wavevector and n is the refractive index of the surrounding medium of the NP. Moreover, α does not only quantify the magnitude of the optical response, but also its phase, a physical quantity of utmost importance in plasmonics [34], or for the design of metasurfaces and meta-atoms [7,8].

Previous studies aiming at retrieving the polarizability of NPs have been reported. Davis and Carney determined the anisotropic polarizability using coherent confocal microscopy [35]. This method allows the estimation of the complex polarizability tensor and the position of the NP. However, the implementation of this method is complex in both the used experimental setup as well as the polarizability retrieval procedure. Celebrano *et al.* determined the amplitude and the phase of the response of single plasmonic particles by combining far-field and near-field imaging [36], but did not measure polarizabilities. Stoller *et al.* reported in 2006 on the measurements of the complex dielectric constant of gold NPs using a differential interference contrast technique [37]. But it only applies for small nanospheres and relies on the preknowledge of the NP diameter.

In this paper, we introduce a procedure based on quantitative phase microscopy aimed at quantifying the full optical properties of a NP, namely its complex dipolar polarizability and all the optical cross sections at once. First, we introduce the experimental approach and some experimental imaging concepts, such as the normalized complex transmission image. Then, we introduce the theoretical model to explain how to process intensity and phase images to retrieve the NP optical properties. Finally, we illustrate the procedure with measurements on gold and dielectric NPs, and compare with numerical simulations. We finally highlight the robustness of the technique by showing that the measurements are dependent neither on the microscope focus nor on the objective's numerical aperture (NA).

2. EXPERIMENTAL METHOD

Optical images of particles were acquired using a bright-field transmission microscope and a quadriwave lateral shearing interferometry (QLSI) camera [38] to map the complex transmittance t of the sample containing the NPs. QLSI image measurements result from the prior acquisition of a reference image (t_0), at a free location, before acquiring a transmission image (t) at the location

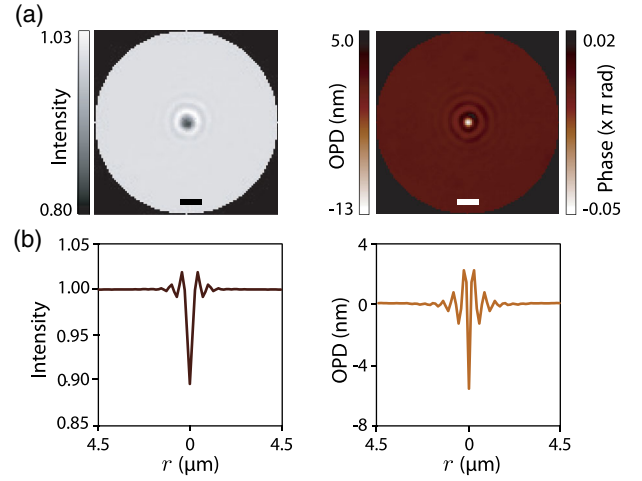


Fig. 1. (a) Intensity (left) and OPD (right) images of a 100 nm gold NP. (b) Radially averaged intensity and OPD profiles (200 \times magnification; 1.3 NA, $\lambda_0 = 530$ nm; scale bar, 1 μm).

of the object of interest [39]. The normalized transmission image t/t_0 is then computed as a means to get rid of any imperfection of the optics of the microscope and of the illumination. We define the normalized complex transmission image t/t_0 as

$$\frac{t}{t_0}(x, y) = \bar{t}(x, y) = \sqrt{T(x, y)} e^{i \frac{2\pi}{\lambda_0} \delta\ell(x, y)}, \quad (4)$$

where $T(x, y)$ is the transmittance image of the sample and $\delta\ell(x, y)$ is the wavefront distortion caused by the presence of the particle or, equivalently, the optical path difference (OPD). $\lambda_0 = 2\pi/k_0$ is the wavelength of the incoming light in vacuum. QLSI enables the mapping of both T and $\delta\ell$ from a single interferogram image (see Fig. S1 in Supplement 1). As an example, we show in Fig. 1 the measured intensity (T) and wavefront distortion ($\delta\ell$) images and their profiles for a 100 nm gold NP embedded in a homogeneous medium. These two images contain the information required to retrieve all the optical properties of the particle, as introduced in the next section.

3. THEORETICAL MODEL

Let us consider a particle, located at \mathbf{r}_0 , excited by an incoming electric field \mathbf{E}_{inc} oscillating at the frequency ω . The resulting oscillating electric dipole \mathbf{p} reads

$$\mathbf{p} = \varepsilon_0 \alpha \mathbf{E}_{\text{inc}}(\mathbf{r}_0), \quad (5)$$

where $\bar{\alpha} = (\alpha_{ij})_{i,j \in \{x,y,z\}}$ is the complex electric dipolar polarizability tensor. If one considers \mathbf{E}_{inc} as a plane wave propagating along z and polarized along x , then left-multiplying Eq. (5) by $\mathbf{E}_{\text{inc}}^*$ yields

$$\alpha_{xx} = \frac{1}{\varepsilon_0 |\mathbf{E}_{\text{inc}}(\mathbf{r}_0)|^2} \mathbf{E}_{\text{inc}}^*(\mathbf{r}_0) \cdot \mathbf{p}. \quad (6)$$

For larger particles, Eq. (6) cannot be used as $\mathbf{E}_{\text{inc}}(\mathbf{r})$ is not necessarily uniform within the particle. Yet, one can still formally define what we shall coin here the *generalized polarizability* along the direction of \mathbf{E}_{inc} , following Eq. (6), as

$$\bar{\alpha} = \frac{1}{\varepsilon_0 |\mathbf{E}_{\text{inc}}|^2} \iiint_V \mathbf{E}_{\text{inc}}^*(\mathbf{r}) \cdot \mathbf{P}(\mathbf{r}) d\mathbf{r}, \quad (7)$$

where \mathbf{P} is the polarization density field within the particle, defining the domain of integration \mathcal{V} . This expression only assumes that \mathbf{E}_{inc} corresponds to a linearly polarized plane wave, so that $|\mathbf{E}_{\text{inc}}|$ is uniform. The benefit of extending the definition of α this way is twofold. (i) The expression Eq. (1) of the extinction cross section using the generalized polarizability Eq. (7) is valid, and is no longer restricted to dipolar NPs, since one retrieves the general expression well known from the discrete dipole approximation (DDA) [40],

$$\sigma_{\text{ext}} = \frac{k}{n\epsilon_0|\mathbf{E}_{\text{inc}}|^2} \iiint_{\mathcal{V}} \Im(\mathbf{E}_{\text{inc}}^*(\mathbf{r}) \cdot \mathbf{P}(\mathbf{r})) d\mathbf{r}. \quad (8)$$

(ii) The quantity defined by Eq. (7) is what we can measure experimentally from intensity and phase images processing. In Supplement 1, we demonstrate that the polarizability of a particle, as defined by Eq. (6) or Eq. (7), can be calculated from its image $\bar{\tau}(x, y)$ through a microscope using the expression

$$\alpha = \frac{i\lambda_0 n}{\pi} \iint (1 - \bar{\tau}(x, y)) dx dy. \quad (9)$$

In practice, this estimation involves a pixel summation over an area of the image that covers all the visible rings of the Airy pattern, as schematized by the following expression:

$$\alpha = \frac{i\lambda_0 n}{\pi} \sum_{\text{pixels}} \left[1 - \sqrt{\text{Airy}} \times \exp\left(i\frac{2\pi}{\lambda_0} \text{Phase}\right) \right] p_{\text{Size}}^2. \quad (10)$$

For the sake of simplicity, this expression assumes a NP embedded in a homogenous medium with a refractive index n , albeit not a requirement. Thus, one can retrieve the real and imaginary parts of the polarizability of any single NP by a processing of the intensity ($T(x, y)$) and wavefront ($\delta\ell(x, y)$) images (PIWI) using

$$\alpha_r = \frac{\lambda_0 n}{\pi} \iint \sqrt{T(x, y)} \sin(k_0 \delta\ell(x, y)) dx dy, \quad (11)$$

$$\alpha_i = \frac{\lambda_0 n}{\pi} \iint \left[1 - \sqrt{T(x, y)} \cos(k_0 \delta\ell(x, y)) \right] dx dy. \quad (12)$$

No assumption is necessary regarding the composition (dielectric, metallic, etc.) of the NP or its shape. Only the preknowledge of the refractive index of the medium, n , and the illumination wavelength λ_0 are required, two easily accessible parameters.

Using Eq. (1) of the extinction cross section as a function of α , one gets

$$\sigma_{\text{ext}} = 2 \iint \left[1 - \sqrt{T(x, y)} \cos(k_0 \delta\ell(x, y)) \right] dx dy. \quad (13)$$

Importantly, this expression is valid for any particle, not necessarily dipolar. This can be derived from the optical theorem, as shown in Supplement 1. PIWI is thus capable of determining α and σ_{ext} for any NP of any composition and geometry, without any preknowledge. However, estimating the scattering and absorption cross sections using Eqs. (2) and (3) remains an approximation, even using the generalized complex polarizability. In practice, the approximation yields correct estimations for NP sizes until typically 100 nm.

4. RESULTS

A. Metal and Dielectric Nanospheres

In order to illustrate the applicability of the PIWI method, we first present measurements on metal and dielectric spherical NPs, at $\lambda_0 = 530$ nm. This simple, isotropic geometry allows us to easily compare our measurements with numerical simulations. Colloidal gold nanospheres of 100 nm in diameter and polystyrene nanospheres of 200 nm in diameter were dispersed on a glass substrate and then covered by glycerol as a means to obtain a homogeneous medium of refractive index 1.5.

An example of measured intensity and OPD images of gold and polystyrene NPs is shown in Fig. 2(a). The measured polarizabilities using PIWI are displayed in the complex plane in Fig. 2(b). Each point corresponds to the polarizability of one NP. The measured polarizabilities for different NPs occupy two separate domains of the complex plane [Fig. 2(a)], associated to gold and polystyrene nanospheres (orange and blue points, respectively). For comparison, we also plot on the same space the calculated complex polarizabilities using DDA for a 100 nm gold nanosphere and a 200 nm polystyrene nanosphere (with gold permittivities taken from Johnson and Christy's dataset [41] and PS permittivities from Ref. [42]). Furthermore, by using the same images, we also extracted the extinction, scattering, and absorption cross sections of the same NPs using PIWI, and compared them with numerical values [Fig. 2(c)], showing a good agreement. Note that the scattering cross section is weak compared with absorption, despite the dielectric nature of the particles, because the particles are immersed in glycerol, leading to a good refractive index matching and making them quasi-transparent. The dispersion in the measured values of the polarizability and the cross sections mainly arises from the dispersion in NP diameters and sometimes shapes (see Fig. S4 in Supplement 1). The measurement errors reported in Figs. 2(d) and 2(e) mainly stem from the shot noise on the camera sensor. Error bars are not displayed in Figs. 2(b) and 2(f) for the sake of readability, but they are displayed in Fig. S6 of Supplement 1.

Spectral measurements of the complex polarizability of 100 nm gold NPs over the entire visible range are shown in Figs. 2(d) and 2(e), with a good agreement with numerical simulations. The imaginary part (proportional to extinction cross section) presents a peak around $\lambda_{\text{res}} = 610$ nm, associated with an abrupt transition of the values of $\text{Re}(\alpha)$, which corresponds to the localized surface plasmon resonance (LSPR) wavelength. From these measurements, optical cross sections were computed using Eqs. (1)–(3) and displayed in Fig. 2(f). The agreement with DDA simulations is good for the extinction cross section. This is consistent with the underlying theory of the experimental approach, which predicts quantitative σ_{ext} measurements, without approximation, for any NP size. The rule does not apply for σ_{sca} and σ_{abs} , for which measurements may deviate from actual values when retardation effects occur. This presumably explains the small deviation between experiments and simulation in the blue–green region of the spectra for σ_{sca} and σ_{abs} observed in Fig. 2(f).

B. Asymmetric Particles

We focus now on the case of anisotropic particles for which the polarizability depends on the illumination polarization angle, to illustrate the versatility of the method. We studied gold nanorods fabricated by nanosphere lithography (see Supplement 1 for more details on the fabrication process) on a glass substrate covered with

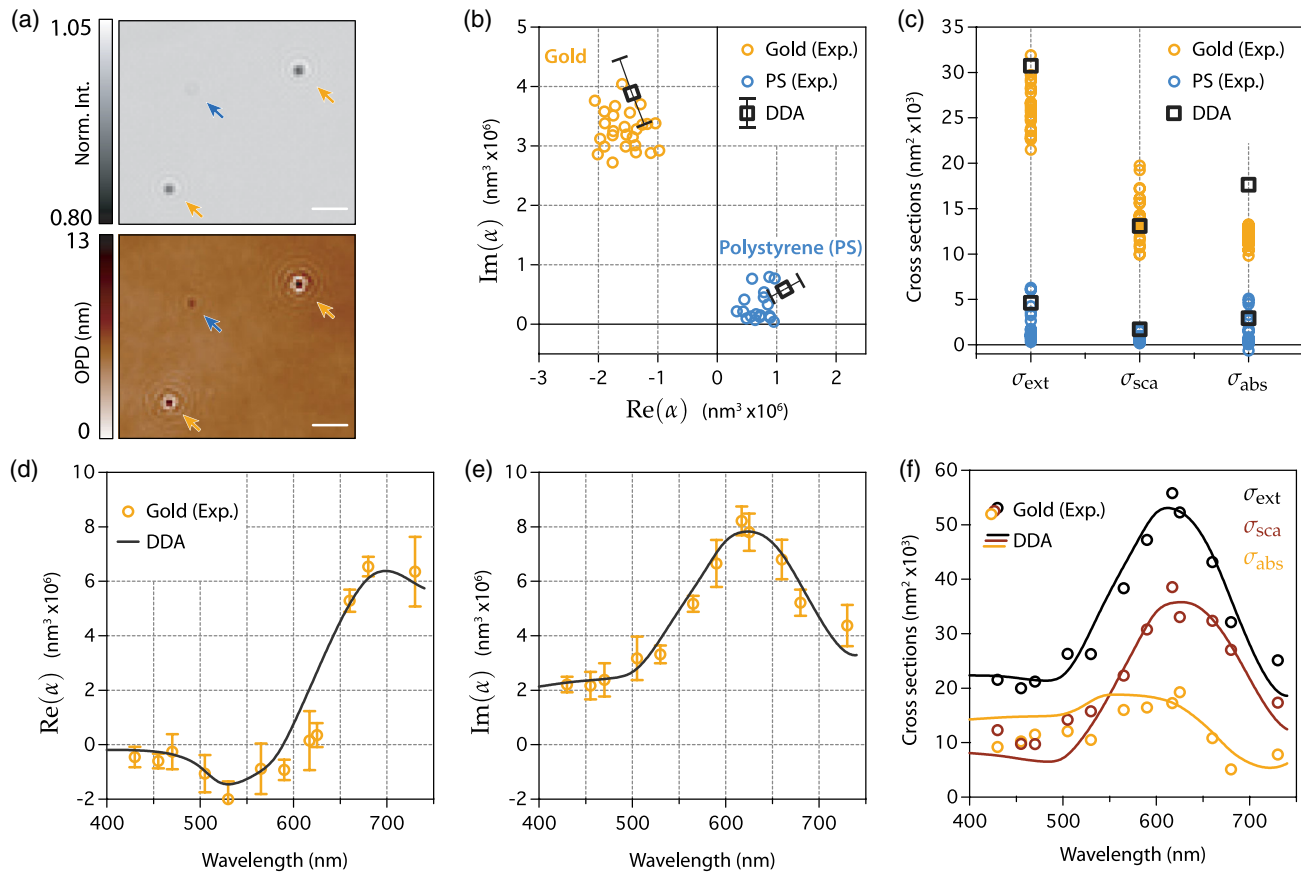


Fig. 2. (a) Intensity and OPD images of 100 nm gold and 200 nm polystyrene beads acquired by QLSI at $\lambda_0 = 530$ nm. Gold and polystyrene are indicated with orange and blue arrows, respectively (100 \times magnification; 1.3 NA; scale bar, 2 μ m). (b) Extracted polarizabilities using PIWI for gold and polystyrene NPs. Squares represent DDA numerical simulations for gold nanoparticles 100 \pm 8 nm in diameter, and PS nanoparticles 200 \pm 16 nm in diameter. (c) Extracted extinction, scattering, and absorption cross sections compared to theoretical values given DDA. Experimental (d) real and (e) imaginary parts of the polarizability of a 100 nm Au nanosphere determined by PIWI (circles), and compared with DDA simulations (solid lines). (f) Cross sections determined from the measured polarizabilities reported in (d) and (e) (circles), and compared with DDA (solid lines).

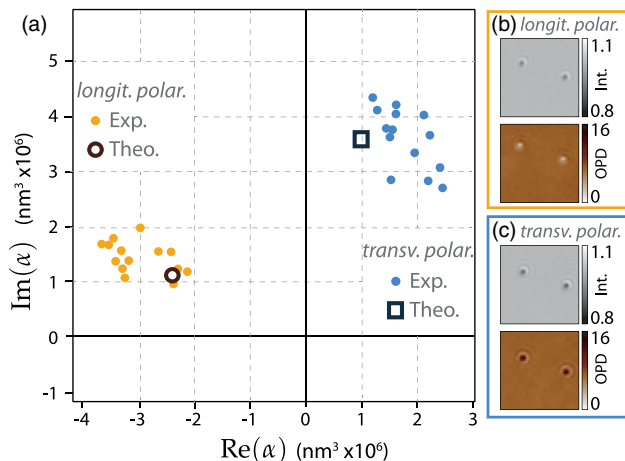


Fig. 3. (a) Measured longitudinal (orange dots) and transverse (blue dots) polarizabilities of a set of gold nanorods compared with theoretical longitudinal (circle symbol) and transverse (square symbol) polarizabilities of nanorods with dimensions of 120 \times 50 \times 50 nm³ in a medium of $n = 1.5$. (b) and (c) Examples of the intensity and OPD images of the nanorods at two different polarization states (100 \times magnification, 1.3 NA).

glycerol. The positions of the nanorods are random, but they all have the same orientation.

The measurements of the polarizability for longitudinal (α_x) and transverse (α_y) illuminations, at $\lambda_0 = 530$ nm, are plotted in Fig. 3(a). Simulated values for a nanorod of 120 nm length, 50 nm width, and 50 nm height embedded in a medium of $n = 1.5$ obtained using DDA are also plotted for comparison. The polarizabilities along the two different axes of the rod occupy two distinct domains in the complex plane with a good agreement with numerical simulations. Note that the geometry used in the numerical simulation consists of a perfect cuboide with sharp corners and flat faces, which is not the case of the fabricated nanorods. The dispersion of the measured values mainly comes from the dispersion of the nanorod dimensions (see Fig. S7 in Supplement 1).

C. No-Effect of the Numerical Aperture and Focus

The effect of the defocus when recording the intensity and OPD images is shown in Fig. 4(a). As expected, the Airy patterns vary substantially as a function of the focus, with even a contrast inversion for the OPD image above and below the focus plane [43]. Yet,

the real and imaginary parts of the polarizability extracted from the intensity and OPD images do not depend on the focus, as shown in Fig. 4(b), and as shown theoretically in Supplement 1 (Section 2). This property makes the measurements particularly robust, since they are independent of any thermal drift of the microscope over time or of any precise focusing of the image.

The effect of the objective's NA is presented in Fig. 4(c). Again, although the diffraction patterns are highly dependent on this parameter [Fig. 4(c)], it surprisingly does not affect the real and imaginary parts of the polarizability extracted using Eq. (10), as plotted in Fig. 4(d). This property is derived in Supplement 1. Again, this independence of the particular objective NA makes the measurements of particle polarizabilities using PIWI particularly robust. No care has to be used regarding the quality of the image and the focus.

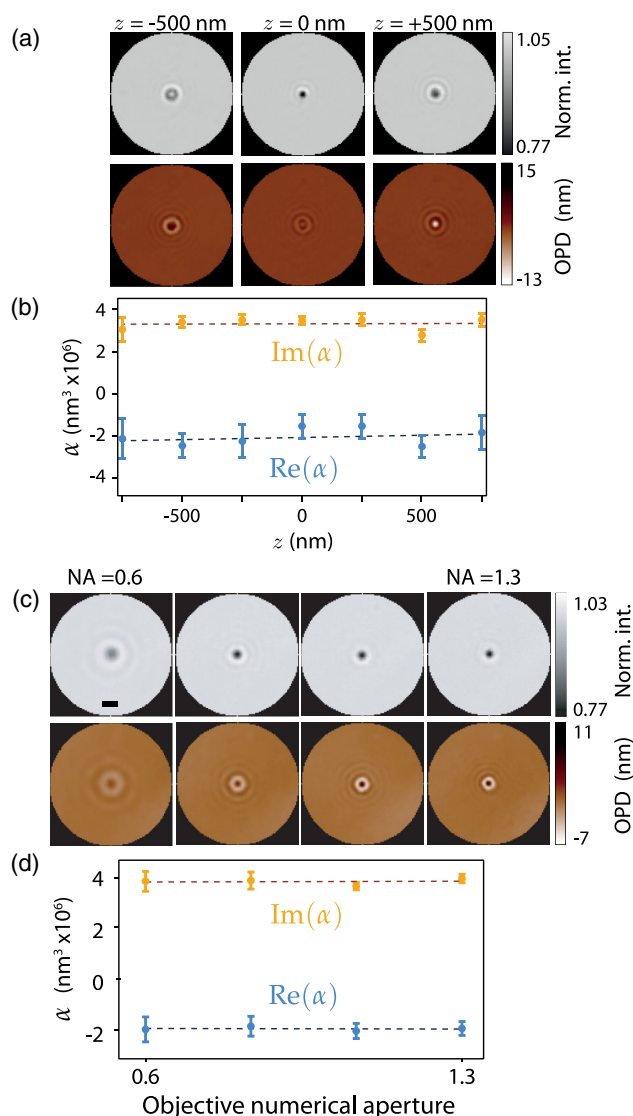


Fig. 4. (a) Intensity and OPD images of a 100 nm gold NP at different z positions, along with their profiles. (b) Extracted real and imaginary parts of the polarizability for different z positions showing no effect of the focus of the microscope on the measurements (scale bar, 1 μm). (c) Intensity and OPD images of a 100 nm gold nanoparticle recorded with different numerical apertures (NA) of the microscope objective. (d) Corresponding real and imaginary parts of the polarizability as a function of NA.

5. CONCLUSION

We reported in this article an experimental method allowing the retrieval of the complex polarizability and optical cross sections of NPs, in a single image acquisition without any assumption on their nature and geometry. The measurements depend neither on the focus of the microscope nor on the NA of the objective lens, making the measurements particularly robust. The complex optical polarizability is measured quantitatively with no assumption, no matter the composition or shape of the particle, and without preknowledge on the system. Absorption and scattering cross sections are only measured approximatively, with a satisfactory estimation for particle sizes typically below 100 nm. This technique is envisioned to become a standard in metrology for nanophotonics, for instance for the active search and characterization of new materials with relevant properties for heterogeneous chemistry, photovoltaics, biosensing, or thermoplasmonics.

Funding. European Research Council (772725); Chalmers Excellence Initiative Nano.

Acknowledgment. This project has received funding from the European Research Council (ERC) under the European Union's Horizon 2020 Research and Innovation Programme (grant agreement no. 772725, project HiPhore) and from Chalmers Excellence Initiative Nano.

Disclosures. The authors declare no conflicts of interest.

See Supplement 1 for supporting content.

REFERENCES

- U. C. Fischer, A. Dereux, and J.-C. Weeber, *Controlling Light Confinement by Excitation of Localized Surface Plasmons* (Springer, 2001), pp. 49–69.
- D. Cialla, A. März, R. Böhme, F. Theil, K. Weber, M. Schmitt, and J. Popp, "Surface-enhanced Raman spectroscopy (SERS): progress and trends," *Anal. Bioanal. Chem.* **403**, 27–54 (2012).
- E. Stratakis and E. Kymakis, "Nanoparticle-based plasmonic organic photovoltaic devices," *Mater. Today* **16**(4), 133–146 (2013).
- G. Vasquez, Y. Hernández, and Y. Coello, "Portable low-cost instrumentation for monitoring Rayleigh scattering from chemical sensors based on metallic nanoparticles," *Sci. Rep.* **8**, 14903 (2018).
- G. Baffou and R. Quidant, "Thermo-plasmonics: using metallic nanostructures as nano-sources of heat," *Laser Photon. Rev.* **7**, 171–187 (2013).
- J. Langer, D. J. de Aberasturi, J. Aizpurua, R. A. Alvarez-Puebla, B. Auguie, J. J. Baumberg, G. C. Bazan, S. E. J. Bell, A. Boisen, A. G. Brolo, J. Choo, D. Cialla-May, V. Deckert, L. Fabris, K. Faulds, F. J. Garcia de Abajo, R. Goodacre, D. Graham, A. J. Haes, C. L. Haynes, C. Huck, T. Itoh, M. Käll, J. Kneipp, N. A. Kotov, H. Kuang, E. C. Le Ru, H. K. Lee, J.-F. Li, X. Y. Ling, S. A. Maier, T. Mayerhöfer, M. Moskovits, K. Murakoshi, J.-M. Nam, S. Nie, Y. Ozaki, I. Pastoriza-Santos, J. Perez-Juste, J. Popp, A. Pucci, S. Reich, B. Ren, G. C. Schatz, T. Shegai, S. Schlucker, L.-L. Tay, K. G. Thomas, Z.-Q. Tian, R. P. Van Duyne, T. Vo-Dinh, Y. Wang, K. A. Willets, C. Xu, H. Xu, Y. Xu, Y. S. Yamamoto, B. Zhao, and L. M. Liz-Marzán, "Present and future of surface-enhanced Raman scattering," *ACS Nano* **14**, 28–117 (2019).
- J. Babocky, A. Krizova, L. Strbkova, L. Kejik, F. Ligmajer, M. Hron, P. Dvorak, M. Tyc, J. Collakova, V. Krapek, R. Kalousek, R. Chmelik, and T. Sikola, "Quantitative 3D phase imaging of plasmonic metasurfaces," *ACS Photon.* **4**, 1389–1397 (2017).
- Y. Zhao and A. Alù, "Manipulating light polarization with ultrathin plasmonic metasurfaces," *Phys. Rev. B* **84**, 205428 (2011).

9. A. Agrawal, S. H. Cho, O. Zandi, S. Ghosh, R. W. Johns, and D. J. Milliron, "Localized surface plasmon resonance in semiconductor nanocrystals," *Chem. Rev.* **118**, 3121–3207 (2018).
10. P. Patsalas, N. Kalfagiannis, and S. Kassavetis, "Optical properties and plasmonic performances of titanium nitride," *Materials* **8**, 3128–3154 (2015).
11. U. Guler, V. M. Shalaev, and A. Boltasseva, "Nanoparticle plasmonics: going practical with transition metal nitrides," *Mater. Today* **18**(4), 227–237 (2015).
12. A. Lalis, G. Tessier, J. Plain, and G. Baffou, "Plasmonic efficiencies of nanoparticles made of metal nitrides (tin, zrn) compared with gold," *Sci. Rep.* **6**, 38647 (2016).
13. M. G. Blaber, M. D. Arnold, N. Harris, M. J. Ford, and M. B. Cortie, "Plasmon absorption in nanospheres: a comparison of sodium, potassium, aluminium, silver and gold," *Phys. B (Amsterdam)* **394**, 184–187 (2007).
14. F. Sterl, N. Strohhfeldt, R. Walter, R. Griessen, A. Tittl, and H. Giessen, "Magnesium as novel material for active plasmonics in the visible wavelength range," *Nano Lett.* **15**, 7949–7955 (2015).
15. M. G. Blaber, M. D. Arnold, and M. J. Ford, "Optical properties of intermetallic compounds from first principles calculations: a search for the ideal plasmonic material," *J. Phys. Condens. Matter* **21**, 144211 (2009).
16. M. G. Blaber, M. D. Arnold, and M. J. Ford, "A review of the optical properties of alloys and intermetallics for plasmonics," *J. Phys. Condens. Matter* **22**, 143201 (2010).
17. S. Link, Z. L. Wang, and M. A. El-Sayed, "Alloy formation of gold-silver nanoparticles and the dependence of the plasmon absorption on their composition," *J. Phys. Chem. B* **103**, 3529–3533 (1999).
18. R. He, Y.-C. Wang, X. Wang, Z. Wang, G. Liu, W. Zhou, L. Wen, Q. Li, X. Wang, X. Chen, J. Zeng, and J. G. Hou, "Facile synthesis of pentacle gold-copper alloy nanocrystals and their plasmonic and catalytic properties," *Nat. Commun.* **5**, 4327 (2014).
19. D. G. Baranov, D. A. Zuev, S. I. Lepeshov, O. V. Kotov, A. E. Krasnok, A. B. Evlyukhin, and B. N. Chichkov, "All-dielectric nanophotonics: the quest for better materials and fabrication techniques," *Optica* **4**, 814–825 (2017).
20. A. Lalis, G. Tessier, J. Plain, and G. Baffou, "Quantifying the efficiency of plasmonic materials for near-field enhancement and photothermal conversion," *J. Phys. Chem. C* **119**, 25518–25528 (2015).
21. V. P. Drachev, U. K. Chettiar, A. V. Kildishev, H.-K. Yuan, W. Cai, and V. M. Shalaev, "The Ag dielectric function in plasmonic metamaterials," *Opt. Express* **16**, 1186–1195 (2008).
22. A. Comin and L. Manna, "New materials for tunable plasmonic colloidal nanocrystals," *Chem. Soc. Rev.* **43**, 3957–3975 (2014).
23. G. L. Hornyak, C. J. Patrissi, E. B. Oberhauser, C. R. Martin, J.-C. Valmalette, L. Lemaire, J. Dutta, and H. Hofmann, "Effective medium theory characterization of Au/Ag nanoalloy-porous alumina composites," *Nanostruct. Mater.* **9**, 571–574 (1997).
24. A. Arbouet, D. Christofilos, N. Del Fatti, F. Vallée, J. R. Huntzinger, L. Arnaud, P. Billaud, and M. Broyer, "Direct measurement of the single-metal-cluster optical absorption," *Phys. Rev. Lett.* **93**, 127401 (2004).
25. M. A. van Dijk, A. L. Tchegbotareva, M. Orrit, M. Lippitz, S. Berciaud, D. Lasne, L. Cognet, and B. Lounis, "Absorption and scattering microscopy of single metal nanoparticles," *Phys. Chem. Chem. Phys.* **8**, 3486–3495 (2006).
26. P. Berto, E. Bermúdez Ureña, P. Bon, R. Quidant, H. Rigneault, and G. Baffou, "Quantitative absorption spectroscopy of nano-objects," *Phys. Rev. B* **86**, 165417 (2012).
27. A. Tcherniak, J. W. Ha, S. Dominguez-Medina, L. S. Slaughter, and S. Link, "Probing a century old prediction one plasmonic particle at a time," *Nano Lett.* **10**, 1398–1404 (2010).
28. M. Husnik, S. Linden, R. Diehl, J. Niegemann, K. Busch, and M. Wegener, "Quantitative experimental determination of scattering and absorption cross-section spectra of individual optical metallic nanoantennas," *Phys. Rev. Lett.* **109**, 233902 (2012).
29. S. D. Gennaro, Y. Sonnerfraud, N. Verellen, P. Van Dorpe, V. V. Moshchalkov, S. A. Maier, and R. F. Oulton, "Spectral interferometric microscopy reveals absorption by individual optical nanoantennas from extinction phase," *Nat. Commun.* **5**, 3748 (2014).
30. S. A. Mann, B. Sciacca, Y. Zhang, J. Wang, E. Kontoleta, H. Liu, and E. C. Garnett, "Integrating sphere microscopy for direct absorption measurements of single nanostructures," *ACS Nano* **11**, 1412–1418 (2017).
31. J. Grand, B. Auguie, and E. C. Le Ru, "Combined extinction and absorption UV-visible spectroscopy as a method for revealing shape imperfections of metallic nanoparticles," *Anal. Chem.* **91**, 14639–14648 (2019).
32. A. Zilli, W. Langbein, and P. Borri, "Quantitative measurement of the optical cross sections of single nano-objects by correlative transmission and scattering microspectroscopy," *ACS Photon.* **6**, 2149–2160 (2019).
33. V. Myroshnychenko, J. Rodríguez-Fernández, I. Pastoriza-Santos, A. M. Funston, C. Novo, P. Mulvaney, L. M. Liz-Marzán, and F. J. García de Abajo, "Modeling the optical response of gold nanoparticles," *Chem. Soc. Rev.* **37**, 1792–1805 (2008).
34. P. S. Carney, B. Deutsch, A. A. Govyadinov, and R. Hillenbrand, "Phase in nanooptics," *ACS Nano* **6**, 8–12 (2012).
35. B. J. Davis and P. S. Carney, "Robust determination of the anisotropic polarizability of nanoparticles using coherent confocal microscopy," *J. Opt. Soc. Am. A* **25**, 2102–2113 (2008).
36. M. Celebrano, M. Savoini, P. Biagioni, M. Zavelani-Rossi, P. M. Adam, L. Duò, G. Cerullo, and M. Finazzi, "Retrieving the complex polarizability of single plasmonic nanoresonators," *Phys. Rev. B* **80**, 153407 (2009).
37. P. Stoller, V. Jacobsen, and V. Sandoghdar, "Measurement of the complex dielectric constant of a single gold nanoparticle," *Opt. Lett.* **31**, 2474–2476 (2006).
38. P. Bon, G. Maucort, B. Wattellier, and S. Monneret, "Quadrivave lateral shearing interferometry for quantitative phase microscopy of living cells," *Opt. Express* **17**, 13080–13094 (2009).
39. S. Khadir, P. C. Chaumet, G. Baffou, and A. Sentenac, "Quantitative model of the image of a radiating dipole through a microscope," *J. Opt. Soc. Am. A* **36**, 478–484 (2019).
40. B. T. Draine and P. J. Flatau, "Discrete-dipole approximation for scattering calculations," *J. Opt. Soc. Am. A* **11**, 1491–1499 (1994).
41. P. B. Johnson and R. W. Christy, "Optical constants of the noble metals," *Phys. Rev. B* **6**, 4370 (1972).
42. R. H. French, K. I. Winey, M. K. Yang, and W. Qiu, "Optical properties and van der Waals-London dispersion interactions of polystyrene determined by vacuum ultraviolet spectroscopy and spectroscopic ellipsometry," *Aust. J. Chem.* **60**, 251–263 (2007).
43. P. Bon, N. Bourg, S. Lécart, S. Monneret, E. Fort, J. Wenger, and S. Léveque-Fort, "Three-dimensional nanometre localization of nanoparticles to enhance super-resolution microscopy," *Nat. Commun.* **6**, 7764 (2015).